

Temperature Dependent Spin-Phonon Coupling of Boron-Vacancy Centers in Hexagonal Boron Nitride

Zhongyuan Liu,^{1,*} Ruotian Gong,^{1,*} Benchen Huang,^{2,*} Yu Jin,² Xinyi Du,¹ Guanghui He,¹ Eli Janzen,³ Li Yang,¹ Erik Henriksen,¹ James Edgar,³ Giulia Galli,^{2,4,5} Chong Zu^{1,6,7,†}

¹Department of Physics, Washington University, St. Louis, MO 63130, USA

²Department of Chemistry, University of Chicago, IL 60637, USA

³Tim Taylor Department of Chemical Engineering, Kansas State University, Manhattan, KS, 66506, USA

⁴Pritzker School of Molecular Engineering, University of Chicago, IL 60637, USA

⁵Material Science Division, Argonne National Lab, IL 60439, USA

⁶Center for Quantum Leaps, Washington University, St. Louis, MO 63130, USA

⁷Institute of Materials Science and Engineering, Washington University, St. Louis, MO 63130, USA

*These authors contributed equally to this work

†To whom correspondence should be addressed; E-mail: zu@wustl.edu

(Dated: April 25, 2024)

The negatively charged boron-vacancy center (V_B^-) in hexagonal boron nitride (hBN) has recently emerged as a highly promising quantum sensor. Compared to the nitrogen-vacancy (NV) center in diamond, the change with temperature of the spin transition energy of V_B^- is more than an order of magnitude larger, making it a potential nanoscale thermometer with superior sensitivity. However, the underlying mechanism of the observed large temperature dependence remains an open question. In this work, using isotopically purified $h^{10}B^{15}N$, we systematically characterize the zero-field splitting, hyperfine interaction, and spin relaxation time of V_B^- from 10 to 350 K. We carry out first-principle calculations of the V_B^- spin-phonon interaction and show that a second-order effect from finite-temperature phonon excitations is responsible for the observed changes in experiments. By fitting our experimental results to a physically motivated model, we extract the dominant phonon mode which agrees well with our simulations. Finally, we investigate the dynamic nuclear spin polarization process at cryogenic temperatures. Our results provide key insights in V_B^- centers and their utilization as nanoscale thermometers and phonon sensors.

Introduction—Optically-addressable solid state spin defects are promising platforms for quantum applications [1–24], and when residing in atomically-thin van der Waals materials they may exhibit properties superior to those of their counterparts in three-dimensional materials [25–29]. Among a wide-range of contestants, the negatively charged boron-vacancy center, V_B^- , in hexagonal boron nitride (hBN) has attracted much growing interest [30–43]. Several interesting properties of the host material, including the large bandgap and excellent stability, as well as the readily controllable spin degree of freedom at room temperature, makes V_B^- in hBN well-suited as a platform for technologies.

When compared with its three-dimensional counterparts, for example the nitrogen-vacancy (NV) center in diamond, the ground state zero-field splitting (ZFS) of V_B^- exhibits a ~ 25 times larger variation from cryogenic to room temperatures, placing it in an advantageous position for nanoscale thermometry [44–48]. However, the underlying mechanism of such a large temperature response remains an open question. In particular, the first-order lattice displacement of hBN with temperature can only account for a negligible fraction of the changes in the measured ZFS of V_B^- [46]; higher-order spin-phonon interactions should be included to quantitatively capture the experimental results.

In this letter, we experimentally characterize the tem-

perature dependence of the ZFS, hyperfine interaction, and spin relaxation time T_1 of V_B^- in isotopically purified $h^{10}B^{15}N$. Compared to conventional hBN with natural abundant ^{14}N , our $h^{10}B^{15}N$ offers much narrower V_B^- spin transitions and substantially improved measurement resolution [49–52]. We then carry out first-principle calculations of the temperature-induced phonon-mediated interaction of V_B^- , motivated by recent investigations of the NV centers in diamond [53, 54]. Our combined experimental and theoretical study allows for the identification of the main mechanism responsible for the observed temperature dependence of the properties of V_B^- , namely a second-order spin-phonon coupling with a characteristic phonon mode energy around 18 meV. We also investigate the dynamic nuclear spin polarization of the nearest three ^{15}N and find that the polarization persists down to 10 K.

Experimental system—The V_B^- is an atomic spin defect in the hBN lattice (Fig. 1a). The electronic ground state of V_B^- exhibits a spin-1 triplet with $|m_s = 0\rangle$ and $|m_s = \pm 1\rangle$. In the absence of external fields, the $|m_s = \pm 1\rangle$ are degenerated and separated from $|m_s = 0\rangle$ by a zero-field splitting (ZFS) $D = (2\pi) \times 3.48$ GHz at room temperature (Fig. 1b).

The Hamiltonian governing V_B^- and the nearest three

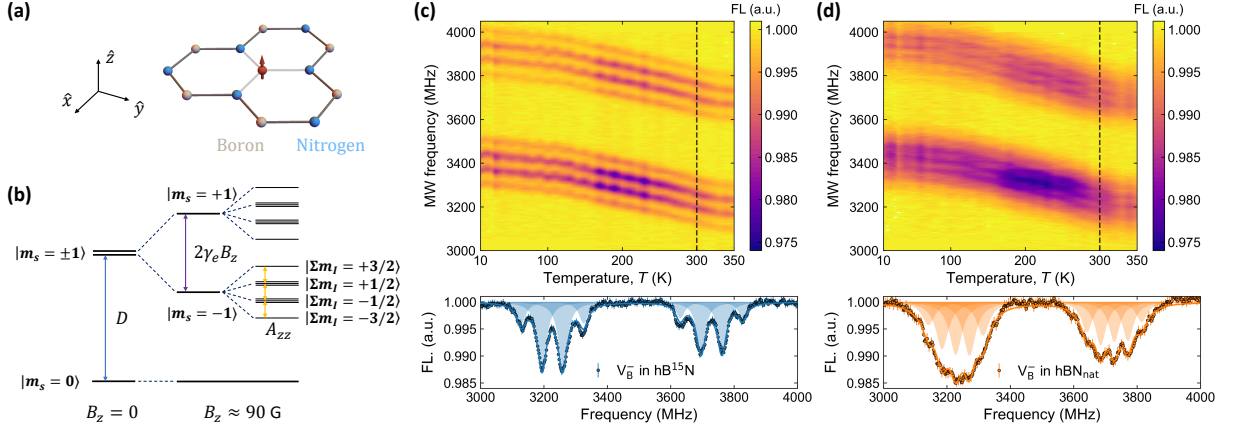


FIG. 1. **Temperature dependence of optically detected magnetic resonance spectra of V_B^- .** (a) Schematic representation of a single V_B^- center (red spin) in the hBN honeycomb lattice. \hat{z} is defined as the out-of-plane direction, while \hat{x} and \hat{y} live in the lattice plane. (b) The V_B^- electronic ground state energy level diagram with the presence of three nearest ^{15}N nuclear spins in isotopically purified $h^{10}B^{15}N$ flakes. The $|m_s = \pm 1\rangle$ is separated from $|m_s = 0\rangle$ by a zero-field splitting D . The hyperfine interaction further divides each spin transition into four transitions with spacing A_{zz} and degeneracy of $\{1, 3, 3, 1\}$. (c) ODMR spectrum of V_B^- in $h^{10}B^{15}N$ flakes under magnetic field $B_z \approx 90$ G at temperatures ranging from 10 K to 350 K. The normalized fluorescence (FL) contrast is marked in the colorbar. The bottom panels of (c) and (d) display the ODMR spectrum at 300 K, corresponding to the black dashed line on the top panels. The spectrum is fitted with two groups of equally spaced Lorentzians to extract the values of ZFS and hyperfine splitting. (d) ODMR spectrum of V_B^- in hBN_{nat} flakes in the 10-350 K temperature range.

nitrogen nuclear spins takes the form,

$$\mathcal{H} = DS_z^2 + \gamma_e B_z S_z + \sum_{j=1}^3 \mathbf{S} \mathbf{A}^j \mathbf{I}^j - \sum_{j=1}^3 \gamma_n B_z I_z^j, \quad (1)$$

where B_z is an external magnetic field along the c -axis of hBN (or \hat{z} direction), \mathbf{S} and S_z are the electron spin-1 operators, \mathbf{I}^j and I_z^j are the nuclear spin operators, and \mathbf{A}^j is the hyperfine tensor coupling electronic and nuclear spins. The factors $\gamma_e = (2\pi) \times 2.8$ MHz/G and γ_n are electronic and nuclear gyromagnetic ratios.

Throughout our experiment, the external magnetic field is $B_z \lesssim 760$ G. In this case, the energy splittings between $|m_s = 0\rangle$ and $|m_s = \pm 1\rangle$ sub-levels, $D \pm \gamma_e B_z$, are much larger than the strength of the hyperfine interaction $|\mathbf{A}^j|$, thus the secular approximation can be adopted: $\sum_j \mathbf{S} \mathbf{A}^j \mathbf{I}^j \approx \sum_j A_{zz}^j S_z I_z^j = A_{zz} (\sum_j I_z^j) S_z$, leading to a nuclear spin dependent energy shift of the electronic transition. This results in $2\mathcal{I} + 1$ transitions between $|m_s = 0\rangle$ and $|m_s = -1\rangle$ (or $|m_s = +1\rangle$) sub-levels, where $\mathcal{I} = \sum_j I^j$ is the total nuclear spin number accounting for all three nearest nitrogen atoms (Fig. 1b).

The corresponding spin transitions of V_B^- can be probed via optically detected magnetic resonance (ODMR) spectroscopy: by sweeping the frequency of the applied microwave drive while monitoring the fluorescence signal of V_B^- , we expect a fluorescence drop whenever the microwave is resonant with an electronic spin transition. We report measurements for hBN with naturally distributed isotopes hBN_{nat} (99.6% ^{14}N with $I = 1$), and for the isotope-engineered $h^{10}B^{15}N$ (99.7%

^{15}N with $I = \frac{1}{2}$) [49, 50]. For conventional hBN_{nat} , there are in total seven broad hyperfine spin transitions; while for $h^{10}B^{15}N$, we observe four sharp resonances, enabling the measurement of ZFS and hyperfine splitting, A_{zz} , with substantially improved resolution (Fig. 1cd).

Experiment results— To investigate the temperature-dependent spin properties of V_B^- , we load hBN samples with thickness ranging from $\sim 30 - 70$ nm into a closed-cycle optical cryostat (Fournine Design) for temperature control from 10 – 350 K. A small external magnetic field $B_z \approx 90$ G is used to lift the degeneracy between $|m_s = \pm 1\rangle$. Figure 1c,d show the ODMR spectra as a function of temperature. We fit the spectra with two groups of equally spaced Lorentzians, corresponding to $|m_s = \pm 1\rangle \leftrightarrow |m_s = 0\rangle$ transition respectively. The ZFS, $D(T)$, can be extracted from the average frequency of the two transition groups, while the hyperfine splitting, $A_{zz}(T)$, is obtained from the fitted spacing between adjacent resonances in each group (Fig. 2a). In addition, we also perform spin relaxation measurements and extract the T_1 timescale of the sample under different temperatures (Fig. 2b).

We find that the ZFS of V_B^- exhibits a dramatic change of more than 200 MHz from 10 to 350 K, which is around 30 times larger than the change observed for NV centers [53]. We determine the susceptibility of V_B^- at room temperature, $\chi(T = 300$ K), to be -880 ± 65 kHz/K for hBN_{nat} , and -784 ± 35 kHz/K for $h^{10}B^{15}N$. These results highlight the potential use of V_B^- as an ultra-sensitive nanoscale thermometer. Furthermore, within

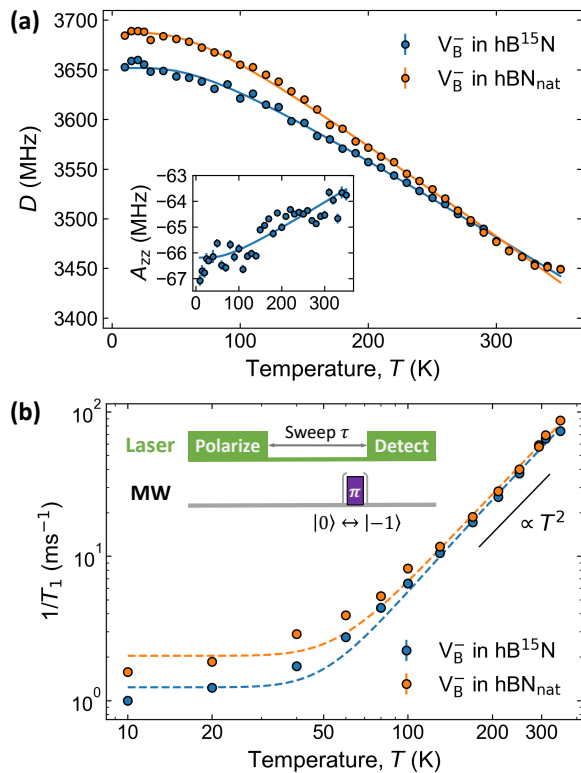


FIG. 2. **Temperature-dependent properties of V_B^- in different hBN samples.** (a) The temperature dependence of the ZFS $D(T)$ of V_B^- in the range 10-350 K. The solid lines represent a fit to a physically motivated model using Eq. 3. Inset: hyperfine interaction $A_{zz}(T)$ of V_B^- in $h^{10}B^{15}N$ within the same temperature range, fitted by the same model with one fixed phonon energy 18.4 meV extracted from the fit of the ZFS. (b) Spin relaxation rate $1/T_1$ of V_B^- in the temperature range 10-350 K. Setting the phonon energy at $\hbar\omega_{exp}$, the dotted lines qualitatively reproduce the T_1 temperature-dependence by the model Eq. 4. In the high temperature regime, the relaxation rate is approximated by a power-law scaling $1/T_1 \propto T^2$. The experimental T_1 pulse sequence is given in the inset.

our measured temperature range, we observe a slightly smaller change of ZFS in $h^{10}B^{15}N$ compared to hBN_{nat} , which can be ascribed to the fact that the heavier nuclei in $h^{10}B^{15}N$ lead to atomic displacements less sensitive to the temperature change. The isotope effect is further evidenced by the measured T_1 timescales, limited by spin-phonon interaction [31, 55, 56]: for heavier nuclei and thus weaker spin-phonon coupling strength, the T_1 of V_B^- in $h^{10}B^{15}N$ is further extended at lower temperatures. We also note that while it remains a challenge to resolve the hyperfine interaction strength from the broad ODMR spectra of conventional hBN_{nat} [49], the substantially better resolved resonances of $h^{10}B^{15}N$ enable an accurate characterization of $A_{zz}(T)$ (see Supplementary Materials). The measured amplitude of $A_{zz}(T)$ displays a noticeable increase from 64 MHz to 67 MHz with de-

creasing temperature, whereas the hyperfine interaction of NV centers to the nearby nuclear spins has been measured to be nearly constant with temperature [57, 58]. Finally, we observe that the ODMR contrast of V_B^- in both hBN samples reaches a maximum around 210 K and persists to low temperatures, without any substantial quenching. This behaviour is again in opposite to that of the NV center in diamond, whose contrast suffers from a significant drop below 90 K [59–61], hindering its sensing performance at cryogenic temperatures.

Theoretical model— To understand the observed temperature dependence of V_B^- spin properties, we adopt a theoretical model which was originally developed to study NV centers in diamond [54]. In particular, we write the electronic and nuclear spin transitions as the sum of two terms,

$$\nu = \nu_0(a(T)) + \frac{1}{2} \sum_i \frac{\partial^2 \nu}{\partial q_i^2} \frac{\hbar}{M_i \omega_i} \left(\frac{1}{e^{\hbar\omega_i/k_B T} - 1} + \frac{1}{2} \right), \quad (2)$$

where ν is the transition frequency (e.g., ZFS and hyperfine interaction) and $a(T)$ is the lattice constant of hBN as a function of temperature [46], q_i, M_i, ω_i are the normal mode of the crystal, mode-specific effective mass, and frequency, respectively. Here the first-order term, $\nu_0(a(T))$, corresponds to the thermal expansion of the hBN lattice, while the second-order term represents vibrational contributions caused by finite-temperature phonon excitations near the equilibrium geometry.

We carry out first-principle simulations using density functional theory (DFT) [62] with the Perdew-Burke-Ernzerhof (PBE) functional [63] to compute the temperature-dependent hyperfine interaction, $A_{zz}(T)$, between V_B^- and the nearest three ^{15}N nuclei. Interestingly, we find that the variation of the lattice constant with temperature only results in an extremely small change in the magnitude of $A_{zz}(T)$. On the other hand, the second-order term accounts for the effect of temperature on the value of $A_{zz}(T)$ observed experimentally.

Figure 3a shows the calculated second-order derivative of the energy of the crystal for each phonon mode. We find a phonon mode with the largest amplitude at energy around $\hbar\omega_{th} \approx 16$ meV, corresponding to an out-of-plane vibration shown in the inset. The computed temperature dependence of $A_{zz}(T)$ agrees well with our

TABLE I. **Zero-field splitting fitting parameters.** For each isotope, the extracted parameters are averaged over four sets of data in different sample spatial positions (see Supplementary Materials), fitted with same model in Eq. 3. We note that D_0 differs from $D(T=0)$, where $D_0 = D(T=0) - \frac{1}{2}c_D$.

Isotopes	D_0 (MHz)	c_D (MHz)	$\hbar\omega_{exp}$ (meV)
^{15}N	3742 ± 10	-175 ± 13	18.4 ± 1.0
^{14}N	3777 ± 26	-201 ± 42	18.8 ± 2.8

experimental results (Fig. 3b). For a direct comparison with the NV center, we also investigate the phonon mode associated with the hyperfine coupling between the NV center and its first shell ^{13}C nuclear spin [54]. In the case of the NV center, the dominant phonon-mode energy is $\simeq 70$ meV [56, 64], requiring a much higher activation temperature than V_{B}^- . Hence the variation of A_{zz} with temperature is much larger for the V_{B}^- center than that observed for the NV center within the range (10–350 K) investigated in our experiment.

The dominant phonon mode found theoretically at $\hbar\omega_{\text{th}} \approx 16$ meV can also be independently determined by fitting the experimentally measured spin properties to a physically motivated model [53],

$$\nu(T) = \nu_0 + c_\nu \left(\frac{1}{e^{\hbar\omega/kT} - 1} + \frac{1}{2} \right), \quad (3)$$

where $\nu(T=0) = \nu_0 + \frac{1}{2}c_\nu$ is the transition energy (e.g. ZFS D and hyperfine A_{zz}) at 0 K and $n = (e^{\hbar\omega/kT} - 1)^{-1}$ is the occupation number of the phonon mode.

We apply this model to the measured ZFS and hyperfine interaction of V_{B}^- . For ZFS, the observed temperature dependence of $D(T)$ for both $\text{h}^{10}\text{B}^{15}\text{N}$ and hBN_{nat} samples can be accurately fitted using our model, from

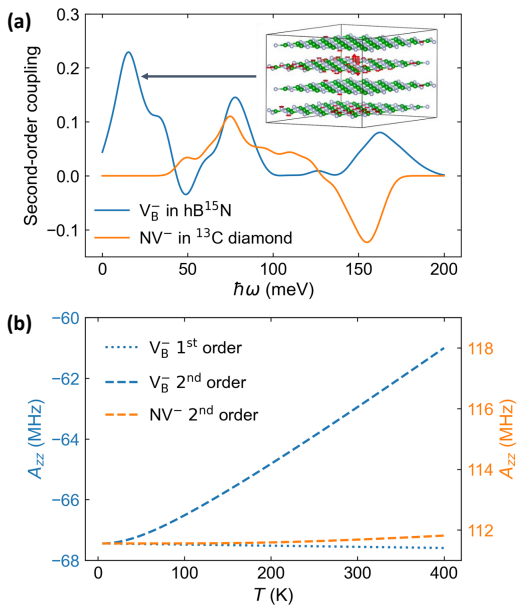


FIG. 3. (a) The second-order vibrational coupling, i.e., $\frac{\partial^2 A_{zz}}{\partial q_i^2} \frac{\hbar}{M_i \omega_i}$ as a function of phonon frequencies of the nearest ^{15}N in hBN (blue) and ^{13}C in diamond (orange) to the vacancy, respectively. The first peak of V_{B}^- in hBN is identified as an out-of-plane vibrational mode (inset). (b) The computed $A_{zz}(T)$ of the nearest ^{15}N in hBN (blue) from both the first and second order vibrational contribution, respectively. We also plotted the computed $A_{zz}(T)$ of the nearest ^{13}C in NV^- in diamond (orange) from the second-order vibrational contribution as a comparison.

which we extract the characteristic phonon energy to be $\hbar\omega_{\text{exp}} = 18.4 \pm 1.0$ meV and 18.8 ± 2.8 meV respectively (Fig. 2a and Table I), in agreement with our theoretical results. The measured hyperfine interaction, $A_{zz}(T)$, shows a temperature dependence that is also consistent with the model with phonon energy set to 18.4 meV (Fig. 2a Inset). Interestingly, the agreement between $\hbar\omega_{\text{exp}}$ and the calculated $\hbar\omega_{\text{th}}$ suggests that the temperature dependence of ZFS and of the hyperfine interaction originate from the coupling of the electronic spin to the same vibrational phonon mode.

We now turn to investigate the temperature dependence of the spin relaxation time T_1 . Within the temperature range (10–350 K) considered here, T_1 of V_{B}^- is dominated by Raman scattering processes, where the energy difference between phonon absorption/emission is equal to the ZFS of V_{B}^- , leading to spin depolarization (see Supplementary Materials) [56]. Therefore the spin relaxation rate of V_{B}^- can be approximated as [56]

$$\Gamma(T) = 1/T_1 \approx An(n+1) + A_S, \quad (4)$$

where $n = (e^{\hbar\omega/kT} - 1)^{-1}$ and A are the phonon occupation number and coupling coefficient associated with the effective mode, and A_S is a sample-related constant that might vary slightly between experiments. Using the phonon energy $\hbar\omega_{\text{exp}} = 18.4$ (18.8) meV determined above, the model of Eq. 4 faithfully reproduces the experimentally measured spin relaxation rates from 50–350 K (Fig. 2b). The small discrepancy below 50 K may be due to the activation of lower-energy phonon modes as well as processes beyond Raman scattering. We note that a prior theoretical study has predicted a power-law scaling of $T_1 \sim T^{-2}$ [65], which is consistent with our experimental results in the high temperature regime (Fig. 2b).

Dynamic nuclear polarization at low temperature— With the temperature-dependent V_{B}^- spin properties in hand, we now turn to investigate the dynamical polarization of the three nearest-neighbor ^{15}N nuclear spins at low temperature. Nuclear spins feature exceptional isolation from noisy environments, making them ideal candidates for quantum storage applications [66, 67]. At room temperature, several prior works have demonstrated the polarization of proximate ^{14}N or ^{15}N with an upper limit of $\sim 30\%$; however how to further improve the polarization fidelity remains an open question [49, 68, 69]. Low temperature offers two potential advantages: $\sim 100\times$ longer V_{B}^- electronic spin lifetime T_1 and stronger hyperfine interaction strength.

To enable resonant spin exchange between electronic and nuclear spins (known as electronic spin level anti-crossing, esLAC) [49, 68, 70], we apply an external magnetic field $B_z \approx 760$ G under which the energy levels corresponding to V_{B}^- excited state $|m_s = 0\rangle$ and $|m_s = -1\rangle$ are nearly degenerate (see Supplementary Materials). We fit the measured hyperfine resonances between $V_{\text{B}}^- |m_s = 0\rangle \leftrightarrow |m_s = +1\rangle$ in the ODMR

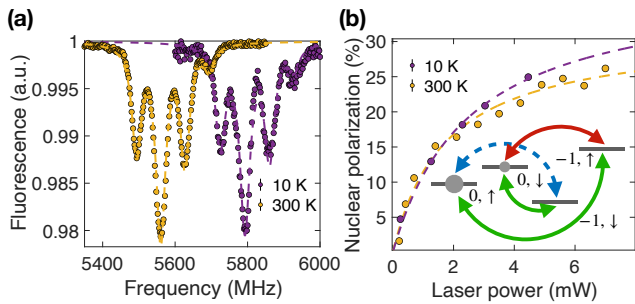


FIG. 4. **Dynamic nuclear polarization at low temperature** (a) Near esLAC level ODMR Spectra of the $|m_s = 0\rangle \leftrightarrow |m_s = -1\rangle$ transition at 10 K and 300 K. The spectra both exhibit similar asymmetry toward the left peaks, indicating a polarization of nuclear spins (see Supplementary Materials) (b) Polarization level of the three nearest ^{15}N nuclear spins near esLAC level as a function of the normalized laser power under room/cryogenic temperature. Inset: schematic representation of the polarization process. The strong spin-conserving optical polarization (green arrow) continuously pumps state from $|m_s = -1\rangle$ to $|m_s = 0\rangle$, and the two hybridisation processes (red arrow and dashed blue arrow) differ in strength, resulting in the polarization of $|m_I = \uparrow\rangle$ state (see Supplementary Materials).

spectra as a function of the laser power to extract the nuclear spin polarization fidelity (Fig. 4a). We find that the nuclear spin polarization at both 10 K and 300 K saturate around 30% with similar laser powers (~ 10 mW) (Fig. 4b), suggesting that the V_B^- spin lifetime T_1 and hyperfine interaction strength are not the limiting sources for nuclear polarization.

The spin polarization may be limited from the spin non-conserving terms in the hyperfine interaction (see Supplementary Materials), which are temperature insensitive. In addition, the observed nuclear spin polarization of V_B^- persists down to 10 K, in sharp contrast to the case of NV centers where the dynamic nuclear polarization process is substantially suppressed at $T \lesssim 50$ K, due to the lack of thermal averaging between NV excited states originating from different orbitals [59, 71]. For V_B^- , the lifting of the double degeneracy of excited states leads to a sufficiently large energy gap between the states, which renders the system insensitive to dynamic Jahn–Teller distortions [70].

Conclusion and Outlook— In summary, our research offers a comprehensive investigation of the temperature-dependent spin-phonon interaction of V_B^- centers in isotopically purified $h^{10}\text{B}^{15}\text{N}$. Our results will be of critical importance in designing experiments to make use of V_B^- centers as nanoscale thermometers and phonon sensors. Moreover, although we focus on V_B^- , the methodologies developed here can be readily applied to a broad family of spin defects in two-dimensional materials [72–75].

Acknowledgements: We gratefully acknowledge Vin-

cent Jacques, Tongcang Li, Shankar Mukherji, Erdong Song, Xi Wang and Norman Yao for helpful discussions. This work is supported by NSF ExpandQISE 2328837 and the Center for Quantum Leaps of Washington University. B. Huang, Y. Jin and G. Galli acknowledge the support of Air Force Office of Scientific Research (AFOSR) under Contract No. FA9550-22-1-0370, the Next Generation Quantum Science and Engineering (QNEXT) hub supported by the U.S. Department of Energy, Office of Science, National Quantum Information Science Research Centers and resources of the University of Chicago Research Computing Center. Support for hBN crystal growth (E. Janzen and J. H. Edgar) was provided by the Office of Naval Research, award no. N00014-22-1-2582.

-
- [1] Kolkowitz, S. *et al.* Coherent sensing of a mechanical resonator with a single-spin qubit. *Science* **335**, 1603–1606 (2012).
 - [2] Doherty, M. W. *et al.* The nitrogen-vacancy colour centre in diamond. *Physics Reports* **528**, 1–45 (2013).
 - [3] Aharonovich, I., Englund, D. & Toth, M. Solid-state single-photon emitters. *Nature Photonics* **10**, 631–641 (2016).
 - [4] Awschalom, D. D., Hanson, R., Wrachtrup, J. & Zhou, B. B. Quantum technologies with optically interfaced solid-state spins. *Nature Photonics* **12**, 516–527 (2018).
 - [5] Atatüre, M., Englund, D., Vamivakas, N., Lee, S.-Y. & Wrachtrup, J. Material platforms for spin-based photonic quantum technologies. *Nature Reviews Materials* **3**, 38–51 (2018).
 - [6] Wolfowicz, G. *et al.* Quantum guidelines for solid-state spin defects. *Nature Reviews Materials* **6**, 906–925 (2021).
 - [7] Togan, E. *et al.* Quantum entanglement between an optical photon and a solid-state spin qubit. *Nature* **466**, 730–734 (2010).
 - [8] Pompili, M. *et al.* Realization of a multinode quantum network of remote solid-state qubits. *Science* **372**, 259–264 (2021).
 - [9] Degen, C. L., Reinhard, F. & Cappellaro, P. Quantum sensing. *Reviews of Modern Physics* **89**, 035002 (2017).
 - [10] Zu, C. *et al.* Emergent hydrodynamics in a strongly interacting dipolar spin ensemble. *Nature* **597**, 45–50 (2021).
 - [11] Koehl, W. F., Buckley, B. B., Heremans, F. J., Calusine, G. & Awschalom, D. D. Room temperature coherent control of defect spin qubits in silicon carbide. *Nature* **479**, 84–87 (2011).
 - [12] Nagy, R. *et al.* High-fidelity spin and optical control of single silicon-vacancy centres in silicon carbide. *Nature Communications* **10**, 1954 (2019).
 - [13] Hensen, B. *et al.* Loophole-free bell inequality violation using electron spins separated by 1.3 kilometres. *Nature* **526**, 682–686 (2015).
 - [14] Randall, J. *et al.* Many-body-localized discrete time crystal with a programmable spin-based quantum simulator. *Science* **374**, 1474–1478 (2021).
 - [15] Hsieh, S. *et al.* Imaging stress and magnetism at high

- pressures using a nanoscale quantum sensor. *Science* **366**, 1349–1354 (2019).
- [16] Thiel, L. *et al.* Probing magnetism in 2d materials at the nanoscale with single-spin microscopy. *Science* **364**, 973–976 (2019).
- [17] Davis, E. *et al.* Probing many-body noise in a strongly interacting two-dimensional dipolar spin system. *Nature Physics* (2023).
- [18] Mittiga, T. *et al.* Imaging the local charge environment of nitrogen-vacancy centers in diamond. *Physical review letters* **121**, 246402 (2018).
- [19] He, G. *et al.* Quasi-floquet prethermalization in a disordered dipolar spin ensemble in diamond. *Physical Review Letters* **131**, 130401 (2023).
- [20] Dwyer, B. L. *et al.* Probing spin dynamics on diamond surfaces using a single quantum sensor. *PRX Quantum* **3**, 040328 (2022).
- [21] Bhattacharyya, P. *et al.* Imaging the meissner effect in hydride superconductors using quantum sensors. *Nature* **627**, 73–79 (2024).
- [22] Acosta, V. M. *et al.* Diamonds with a high density of nitrogen-vacancy centers for magnetometry applications. *Physical Review B* **80**, 115202 (2009).
- [23] de Leon, N. P. *et al.* Materials challenges and opportunities for quantum computing hardware. *Science* **372**, eabb2823 (2021).
- [24] Luo, J., Geng, Y., Rana, F. & Fuchs, G. D. Room temperature optically detected magnetic resonance of single spins in gan. *Nature Materials* 1–7 (2024).
- [25] Azzam, S. I., Parto, K. & Moody, G. Prospects and challenges of quantum emitters in 2d materials. *Applied Physics Letters* **118** (2021).
- [26] Ren, S., Tan, Q. & Zhang, J. Review on the quantum emitters in two-dimensional materials. *Journal of Semiconductors* **40**, 071903 (2019).
- [27] Caldwell, J. D. *et al.* Photonics with hexagonal boron nitride. *Nature Reviews Materials* **4**, 552–567 (2019).
- [28] Naclerio, A. E. & Kidambi, P. R. A review of scalable hexagonal boron nitride (h-bn) synthesis for present and future applications. *Advanced Materials* **35**, 2207374 (2023).
- [29] Ye, M., Seo, H. & Galli, G. Spin coherence in two-dimensional materials. *npj Computational Materials* **5**, 44 (2019).
- [30] Gottscholl, A. *et al.* Initialization and read-out of intrinsic spin defects in a van der waals crystal at room temperature. *Nature Materials* **19**, 540–545 (2020).
- [31] Gottscholl, A. *et al.* Room temperature coherent control of spin defects in hexagonal boron nitride. *Science Advances* **7**, eabf3630 (2021).
- [32] Gong, R. *et al.* Coherent dynamics of strongly interacting electronic spin defects in hexagonal boron nitride. *Nature Communications* **14**, 3299 (2023).
- [33] Huang, M. *et al.* Wide field imaging of van der waals ferromagnet Fe₃GeTe₂ by spin defects in hexagonal boron nitride. *Nature Communications* **13**, 5369 (2022).
- [34] Broadway, D. A. *et al.* Imaging domain reversal in an ultrathin van der waals ferromagnet. *Advanced Materials* **32**, 2003314 (2020).
- [35] Kumar, P. *et al.* Magnetic imaging with spin defects in hexagonal boron nitride. *Physical Review Applied* **18**, L061002 (2022).
- [36] Healey, A. *et al.* Quantum microscopy with van der waals heterostructures. *Nature Physics* **19**, 87–91 (2023).
- [37] Robertson, I. O. *et al.* Detection of paramagnetic spins with an ultrathin van der waals quantum sensor. *ACS Nano* **17**, 13408–13417 (2023).
- [38] Gao, X. *et al.* Quantum sensing of paramagnetic spins in liquids with spin qubits in hexagonal boron nitride. *ACS Photonics* **10**, 2894–2900 (2023).
- [39] Udvarhelyi, P. *et al.* A planar defect spin sensor in a two-dimensional material susceptible to strain and electric fields. *npj Computational Materials* **9**, 150 (2023).
- [40] Hennessey, M. *et al.* Framework for engineering of spin defects in hexagonal boron nitride by focused ion beams. *arXiv preprint arXiv:2303.06784* (2023).
- [41] Patrickson, C. J., Baber, S., Gaál, B. B., Ramsay, A. J. & Luxmoore, I. J. High frequency magnetometry with an ensemble of spin qubits in hexagonal boron nitride. *npj Quantum Information* **10**, 5 (2024).
- [42] Ivády, V. *et al.* Ab initio theory of the negatively charged boron vacancy qubit in hexagonal boron nitride. *npj Computational Materials* **6**, 41 (2020).
- [43] Kianinia, M., White, S., Fröch, J. E., Bradac, C. & Aharonovich, I. Generation of spin defects in hexagonal boron nitride. *ACS photonics* **7**, 2147–2152 (2020).
- [44] Vaidya, S., Gao, X., Dikshit, S., Aharonovich, I. & Li, T. Quantum sensing and imaging with spin defects in hexagonal boron nitride. *Advances in Physics: X* **8**, 2206049 (2023).
- [45] Liu, W. *et al.* Temperature-dependent energy-level shifts of spin defects in hexagonal boron nitride. *ACS Photonics* **8**, 1889–1895 (2021).
- [46] Gottscholl, A. *et al.* Spin defects in hbn as promising temperature, pressure and magnetic field quantum sensors. *Nature Communications* **12**, 4480 (2021).
- [47] Kucsko, G. *et al.* Nanometre-scale thermometry in a living cell. *Nature* **500**, 54–58 (2013).
- [48] Neumann, P. *et al.* High-precision nanoscale temperature sensing using single defects in diamond. *Nano Letters* **13**, 2738–2742 (2013).
- [49] Gong, R. *et al.* Isotope engineering for spin defects in van der waals materials. *Nature Communications* **15**, 104 (2024).
- [50] Janzen, E. *et al.* Boron and nitrogen isotope effects on hexagonal boron nitride properties. *Advanced Materials* 2306033 (2023).
- [51] Clua-Provost, T. *et al.* Isotopic control of the boron-vacancy spin defect in hexagonal boron nitride. *Physical Review Letters* **131**, 126901 (2023).
- [52] Sasaki, K., Taniguchi, T. & Kobayashi, K. Nitrogen isotope effects on boron vacancy quantum sensors in hexagonal boron nitride. *Applied Physics Express* **16**, 095003 (2023).
- [53] Cambria, M. C. *et al.* Physically motivated analytical expression for the temperature dependence of the zero-field splitting of the nitrogen-vacancy center in diamond. *Phys. Rev. B* **108**, L180102 (2023).
- [54] Tang, H., Barr, A. R., Wang, G., Cappellaro, P. & Li, J. First-principles calculation of the temperature-dependent transition energies in spin defects. *The Journal of Physical Chemistry Letters* **14**, 3266–3273 (2023).
- [55] Durand, A. *et al.* Optically active spin defects in few-layer thick hexagonal boron nitride. *Phys. Rev. Lett.* **131**, 116902 (2023).
- [56] Cambria, M. C. *et al.* Temperature-dependent spin-lattice relaxation of the nitrogen-vacancy spin triplet in diamond. *Phys. Rev. Lett.* **130**, 256903 (2023).

- [57] Barson, M. *et al.* Temperature dependence of the c 13 hyperfine structure of the negatively charged nitrogen-vacancy center in diamond. *Physical Review B* **99**, 094101 (2019).
- [58] Xu, S. *et al.* High-precision measurements and first-principles explanation of the temperature-dependent c 13 and n 14 hyperfine interactions of single nv- centers in diamond at room temperature. *Physical Review B* **107**, L140101 (2023).
- [59] Fischer, R., Jarmola, A., Kehayias, P. & Budker, D. Optical polarization of nuclear ensembles in diamond. *Physical Review B* **87**, 125207 (2013).
- [60] Ernst, S., Scheidegger, P. J., Diesch, S., Lorenzelli, L. & Degen, C. L. Temperature dependence of photoluminescence intensity and spin contrast in nitrogen-vacancy centers. *Physical Review Letters* **131**, 086903 (2023).
- [61] Happacher, J. *et al.* Temperature-dependent photo-physics of single nv centers in diamond. *Physical Review Letters* **131**, 086904 (2023).
- [62] Kohn, W. & Sham, L. J. Self-consistent equations including exchange and correlation effects. *Physical Review* **140**, A1133 (1965).
- [63] Perdew, J. P., Burke, K. & Ernzerhof, M. Generalized gradient approximation made simple. *Physical Review Letters* **77**, 3865 (1996).
- [64] Liu, M. *et al.* First-principles investigation of the impact of stress and lattice vibration on the hyperfine interactions of the nitrogen-vacancy center in diamond. *Physical Review B* **108**, 155150 (2023).
- [65] Mondal, S. & Lughni, A. Spin-phonon decoherence in solid-state paramagnetic defects from first principles. *npj Computational Materials* **9**, 120 (2023).
- [66] Bradley, C. E. *et al.* A ten-qubit solid-state spin register with quantum memory up to one minute. *Physical Review X* **9**, 031045 (2019).
- [67] Metsch, M. H. *et al.* Initialization and readout of nuclear spins via a negatively charged silicon-vacancy center in diamond. *Physical Review Letters* **122**, 190503 (2019).
- [68] Gao, X. *et al.* Nuclear spin polarization and control in hexagonal boron nitride. *Nature Materials* **21**, 1024–1028 (2022).
- [69] Ru, S. *et al.* Robust nuclear spin polarization via ground-state level anti-crossing of boron vacancy defects in hexagonal boron nitride. *arXiv preprint arXiv:2306.15960* (2023).
- [70] Mathur, N. *et al.* Excited-state spin-resonance spectroscopy of vb- defect centers in hexagonal boron nitride. *Nature Communications* **13**, 3233 (2022).
- [71] Block, M. *et al.* Optically enhanced electric field sensing using nitrogen-vacancy ensembles. *Physical Review Applied* **16**, 024024 (2021).
- [72] Stern, H. L. *et al.* A quantum coherent spin in a two-dimensional material at room temperature. *arXiv preprint arXiv:2306.13025* (2023).
- [73] Guo, N.-J. *et al.* Coherent control of an ultrabright single spin in hexagonal boron nitride at room temperature. *Nature Communications* **14**, 2893 (2023).
- [74] Li, S., Thiering, G., Udvarhelyi, P., Ivády, V. & Gali, A. Carbon defect qubit in two-dimensional ws2. *Nature Communications* **13**, 1210 (2022).
- [75] Lee, Y. *et al.* Spin-defect qubits in two-dimensional transition metal dichalcogenides operating at telecom wavelengths. *Nature Communications* **13**, 7501 (2022).

Supplementary Information: Temperature Dependent Spin-phonon Coupling of Boron-vacancy Centers in Hexagonal Boron Nitride

Zhongyuan Liu,^{1,*} Ruotian Gong,^{1,*} Benchen Huang,^{2,*} Yu Jin,² Xinyi Du,¹ Guanghui He,¹
Eli Janzen,³ Li Yang,¹ Erik Henriksen,¹ James Edgar,³ Giulia Galli,^{2,4,5} Chong Zu^{1,6,7,†}

¹Department of Physics, Washington University, St. Louis, MO 63130, USA

²Department of Chemistry, University of Chicago, IL 60637, USA

³Tim Taylor Department of Chemical Engineering, Kansas State University, Manhattan, KS, 66506, USA

⁴Pritzker School of Molecular Engineering, University of Chicago, IL 60637, USA

⁵Material Science Division, Argonne National Lab, IL 60439, USA

⁶Center for Quantum Leaps, Washington University, St. Louis, MO 63130, USA

⁷Institute of Materials Science and Engineering, Washington University, St. Louis, MO 63130, USA

*These authors contributed equally to this work

†To whom correspondence should be addressed; E-mail: zu@wustl.edu

(Dated: April 25, 2024)

CONTENTS

I. Experimental Setup	1
II. hBN Device Fabrication	2
II.1. Growth of Isotopically Purified $h^{10}B^{15}N$	2
II.2. Creation of V_B^- defects	2
II.3. Fabrication of Coplanar Waveguide	3
III. Data Analysis	3
III.1. ODMR Spectrum Fitting	3
III.2. ZFS Temperature Dependence Fitting	3
IV. AB INITIO CALCULATION	4
IV.1. Electronic Structure	4
IV.2. Hyperfine Interaction	4
IV.3. Zero Field Splitting	5
IV.4. Spin Relaxation Time	5
V. ODMR Contrast and Microwave Loss	6
VI. Nuclear Spin Polarization	7
VI.1. Interaction Hamiltonian for V_B^- and nuclear spins	7
VI.2. Spin population transfer near esLAC	8
VI.3. Quantifying polarization	8
References	9

I. EXPERIMENTAL SETUP

We characterize the temperature-dependent spin properties of V_B^- center in both $h^{10}B^{15}N$ and hBN_{nat} using a combination of a home-built confocal scanning microscope and a commercial close-cycle cryostat (Fournine Design) with optical access. A 532 nm laser (Millennia eV High Power CW DPSS Laser) is used for V_B^- spins initialization as well as detection. The laser is shuttered by an acousto-optic modulator (AOM, G&H AOMO 3110-120) in a double-pass configuration to achieve $> 10^5 : 1$ on/off ratio. An objective lens (Mitutoyo Plan Apo 20x/0.42 NA) focuses the laser beam to a diffraction-limited spot with diameter less than $1 \mu\text{m}$ and collects the V_B^- fluorescence. The fluorescence is then separated from the laser beam by a dichroic mirror and filtered through a long-pass filter

before being detected by a single photon counting module (Excelitas SPCM-AQRH-63-FC). The signal is processed by a data acquisition device (National Instruments USB-6343). The objective lens is mounted on a piezo objective scanner (Physik Instrumente PD72Z1x PIFO) in order to control the position of the objective and scans the laser beam vertically. The lateral scanning is performed by an X-Y galvanometer (Thorlabs GVS212) with a $4f$ telescope.

The microwave driving field is generated from a signal generator (Stanford Research Systems SG384, SG386), amplified by a high-power amplifier (Mini-Circuits ZHL-15W-422-S+) and shuttered by a switch (Minicircuits ZASWA-2-50DRA+) to prevent any potential leakage. All equipment are gated through a programmable multi-channel pulse generator (SpinCore PulseBlasterESR-PRO 500) with 2 ns temporal resolution.

The cryostat is cooled down to base temperature below 4 K by a closed-cycle helium compressors (Sumitomo F-40L). A cryogenic temperature controller (LakeShore Model 336) and a sample temperature sensor with build-in heaters are used to maintain samples at desired temperature in range from 4 K to 350 K.

II. HBN DEVICE FABRICATION

II.1. Growth of Isotopically Purified $h^{10}B^{15}N$

High-quality $h^{10}B^{15}N$ flakes are grown via precipitation from a molten Ni-Cr flux as detailed in [1]. Ni, Cr, and isotopically pure ^{10}B powders in the mass ratio 12:12:1 [Ni:Cr:B] are first loaded into an alumina crucible, then heated at $1550^{\circ}C$ for 24 hours in a continuously flowing Ar/ H_2 atmosphere to melt all three components into a homogenous ingot and remove oxygen impurities. Next, this ingot is heated at $1550^{\circ}C$ for 24 hours in a static $^{15}N_2/H_2$ atmosphere to saturate the molten flux with ^{15}N , then slowly cooled at $1^{\circ}C/hr$ to precipitate hBN from the solution. Since isotopically pure ($> 99\%$) ^{10}B and ^{15}N are the only sources of boron and nitrogen in the system, the hBN single crystals that precipitated have the same isotopes.

II.2. Creation of V_B^- defects

We first exfoliate hBN nanosheets using tapes and then transfer them onto the Si/SiO₂ wafer. The wafer is pretreated with O₂ plasma at 50 W for 1 minute (flow rate 20 sccm). The tapes and wafers are heated to $100^{\circ}C$ for 1 minute before samples are carefully peeled off for maximum hBN flake yield [2]. The wafers with hBN_{nat} and $h^{10}B^{15}N$ are then sent to CuttingEdge Ions LLC for $^4He^+$ ion implantation with energy 3 keV and dose density 1 ion/nm² to create V_B^- defects. After implantation, the hBN flakes with thickness around 100 nm are transferred onto the coplanar waveguide using polycarbonate (PC) stamps. Specifically, the temperature is raised in a stepwise manner to facilitate the transfer of hBN flakes. After successful transfer, the waveguide is immersed in chloroform for cleaning, removing any residual PC films.

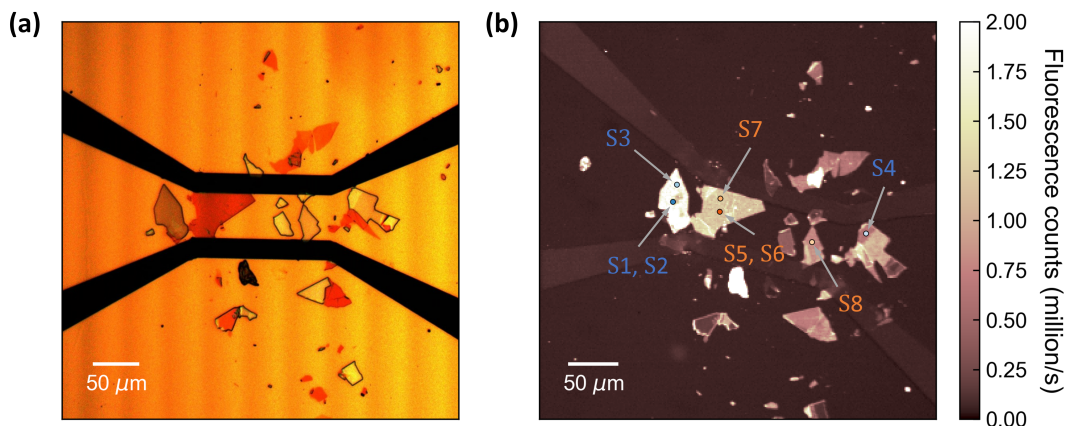


FIG. S1. **Optical and fluorescence images of the hBN flakes.** (a) A optical image of the hBN flakes on the coplanar waveguide. (b) A confocal scanning fluorescence image of the hBN flakes. The eight sets of data taken at six different spacial points are labeled as S1-S8, where S1-S4 are on $h^{10}B^{15}N$ flakes and S5-S8 are on hBN_{nat} flakes.

II.3. Fabrication of Coplanar Waveguide

An impedance-matched (50Ω) coplanar waveguide is fabricated onto a $400 \mu\text{m}$ thick sapphire wafer for microwave delivery (Supplementary Figure S1). Specifically, photoresist layers (LOR 1A/S1805) are first applied to the sapphire wafer at a spin rate 4000 rpm for 1 minute. A carefully designed waveguide pattern with a $50 \mu\text{m}$ wide central line is then developed using a direct-write lithography system (Heidelberg DWL66+), followed by an O_2 plasma cleaning process to remove resist residue. A 8 nm chromium adhesion layer and a 180 nm gold layer are deposited using thermal evaporation, followed by a lift-off process.

III. DATA ANALYSIS

III.1. ODMR Spectrum Fitting

As we discussed in the main text, the resonances of ODMR spectrum can be divided into two groups, corresponding to $|m_s = 0\rangle \leftrightarrow |m_s = -1\rangle$ and $|m_s = 0\rangle \leftrightarrow |m_s = +1\rangle$ transitions respectively. Each group consists of four resonant peaks in $h^{10}\text{B}^{15}\text{N}$ samples and seven peaks in $h\text{BN}_{\text{nat}}$ samples, due to the different nuclear spin numbers in the nitrogen isotopes. Hence, each ODMR spectrum is modeled by two groups of equal-spaced Lorentzian profiles. The fitting parameters of each group are transition frequency, Lorentzian width, and peak amplitude with ratio $1 : 3 : 3 : 1$ for $h^{10}\text{B}^{15}\text{N}$ sample (see section VI.3) or no constraint for $h\text{BN}_{\text{nat}}$ sample. An additional parameter, hyperfine splitting, is included to ascribe the interval between neighboring resonance in one group. As a result, the ZFS, $D(T)$, is extracted from the average of two transition frequencies, while the hyperfine splitting, $A_{zz}(T)$, is directly obtained from the fitting.

III.2. ZFS Temperature Dependence Fitting

We describe the measured ZFS of V_{B}^- using the theoretical phonon model proposed in main text (Equation 3). For both $h^{10}\text{B}^{15}\text{N}$ and $h\text{BN}_{\text{nat}}$ samples, we take four sets of data at different positions on multiple flakes showing in Fig. S1, in order to reduce the experiment error. Each data set is fitted independently with parameters D_0 , c_D , and $\hbar\omega$, and summarized in Fig. S2. The parameters are then be averaged and presented in Table 1 in the main text, with standard deviation across data sets. We denote the averaged fitted value of ZFS at $T = 0$ K of V_{B}^- in $h^{10}\text{B}^{15}\text{N}$ and $h\text{BN}_{\text{nat}}$ flakes with blue and orange shaded area respectively, indicating the different ZFS behaviors of V_{B}^- at very low temperature.

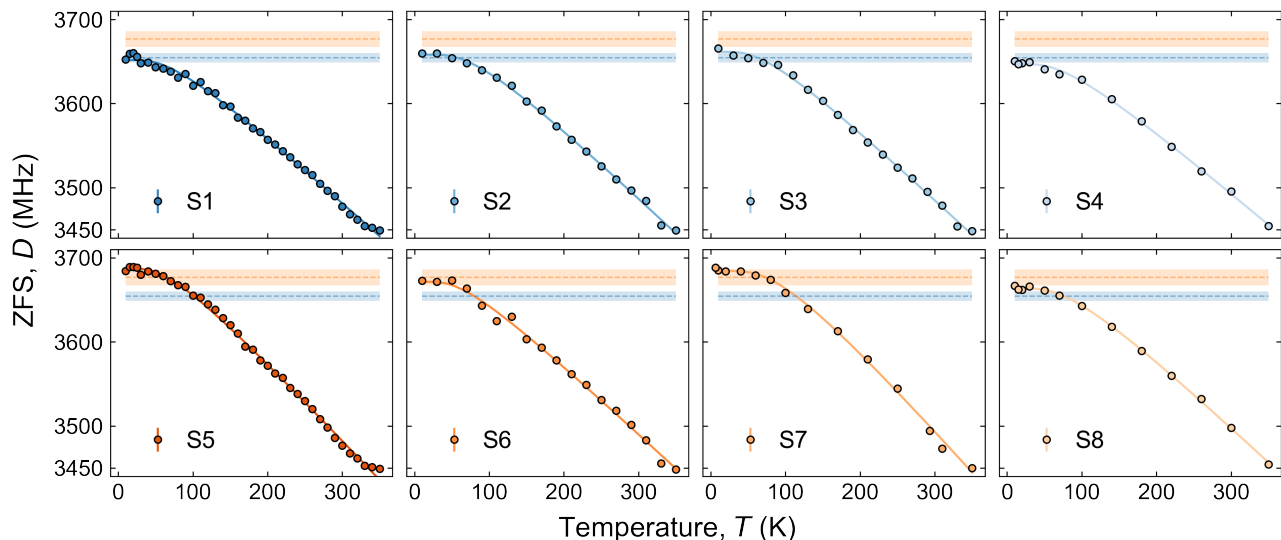


FIG. S2. **Extracted ZFS temperature dependence of V_{B}^- at different spatial points in $h\text{BN}$ flakes.** The average fitted value and corresponding uncertainty of one standard deviation of ZFS at $T = 0$ K of V_{B}^- in $h^{10}\text{B}^{15}\text{N}$ and $h\text{BN}_{\text{nat}}$ flakes are represented as blue and orange shaded area respectively.

IV. AB INITIO CALCULATION

IV.1. Electronic Structure

The electronic structure calculations employ the projector-augmented-wave (PAW) method implemented in the open-source plane-wave-based Quantum ESPRESSO software package (QE) [3, 4] with a kinetic energy cutoff of 75 Ry. Spin-unrestricted calculations are performed using the Perdew-Burke-Ernzerhof (PBE) functional [5] in the computation of relaxed atomic geometries, phonons from the frozen-phonon approach [6], and hyperfine tensor A . The threshold of energy convergence is set to 10^{-8} eV, and that for force on atoms is set to 0.005 eV/Å for geometry optimization calculations.

As discussed in the main text, the temperature dependence can be captured via phonons. We note that for Eq. (2) in the main text, only diagonal terms are considered for the second-order contributions, leaving out the off-diagonal terms. This simplification proves to be good for the study of NV^- center in diamond [7] and V_B^- in hBN.

The phonon calculation for V_B^- in hBN is performed using a 287-atom supercell with only Γ -point sampling. The lattice parameters are taken from experiments at 0 K [8]. A total of 861 phonon modes are obtained, including 3 trivial modes corresponding to translations with no contribution to the temperature dependence. Therefore, all the 858 non-trivial phonon modes are then used to calculate the second-order derivative according to Eq. (2) in the main text, with the step of displacement δq_i set to 0.1 Å.

IV.2. Hyperfine Interaction

The hyperfine interaction between nuclear spin and electron spin includes the isotropic (Fermi contact) term at the nucleus site N and the anisotropic dipole-dipole interaction term near the nucleus site N

$$A_{\text{iso}}(N) = \frac{2\mu_0}{3} g_e \mu_e g_N \mu_N \rho_{\text{spin}}(\mathbf{R}), \quad (\text{S1})$$

$$A_{\text{aniso}}(N) = \frac{\mu_0}{4\pi} g_e \mu_e g_N \mu_N \int d^3r \rho_{\text{spin}}(\mathbf{r}) \frac{3 \cos^2 \theta - 1}{2r^3}, \quad (\text{S2})$$

where μ_0 is the permeability of vacuum, g_e, g_N is the electron and nuclear Landé g-factor, μ_e, μ_N is the Bohr and nuclear magneton. \mathbf{r} is the displacement between the electron and the nucleus at \mathbf{R} . ρ_{spin} denotes the electronic spin density computed from DFT, and θ is the angle between \mathbf{r} and z axis.

The temperature dependence of the full hyperfine tensor of the three nearest ^{15}N atoms computed via the method discussed in the previous subsection are plotted in Fig. S3. Only second-order contribution is considered since the lattice expansion effect is negligible. Note that $A_{yz} = A_{zx} = 0$ due to the point group symmetry of the defect center.

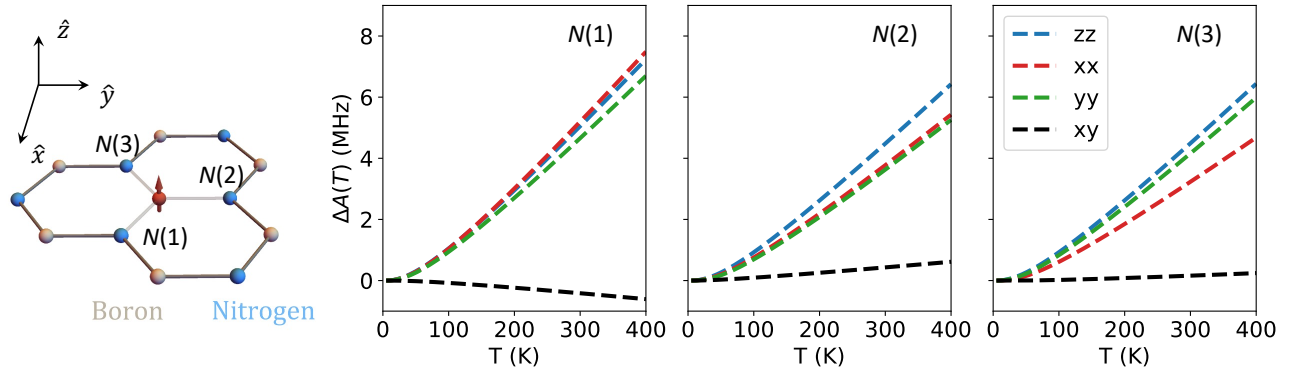


FIG. S3. Temperature dependence of the full hyperfine tensor of three nearest ^{15}N computed from the second-order spin-phonon coupling.

IV.3. Zero Field Splitting

The ZFS originates from the dipolar spin-spin interaction between electrons and can be computed as

$$D_{ab} = \frac{\mu_0 g_e^2 \mu_e^2}{4\pi} \sum_{i < j}^{\text{occ.}} \chi_{ij} \left\langle \Psi_{ij} \left| \frac{r^2 \delta_{ab} - 3r_a r_b}{r^5} \right| \Psi_{ij} \right\rangle, \quad (\text{S3})$$

where $|\Psi_{ij}\rangle$ represents a two-particle Slater determinant constructed from the Kohn-Sham ground state and $\chi_{ij} = \pm 1$ when i, j have the same/different spins. And the summation runs over all the possible electron pairs.

It has been noted by Ivády et al. [9] that it's necessary to apply hybrid functionals [10] to a 971-atom supercell, together with a post-correction for spin contamination [11], to obtain a reasonable estimation of ZFS. This calculation is computationally expensive and impractical for the investigation of temperature dependencies, which involves hundreds of single point calculations.

To qualitatively understand this temperature dependence, we focus on the coupling between spin and local phonon modes around the V_B^- center. Specifically, we cut a cluster (passivated with hydrogen atoms) with 7.5 Å radius [12] from the supercell, and apply local phonon displacements on top of it. Then we performed DFT calculations with the PBE0 [13] functional and the def2-SVP basis set to compute the ground state and the ZFS using the ORCA package [14], and the results are shown in Fig. S4. It can be noticed that the absolute values of the computed ZFS and the magnitude of the variation as a function of temperature are underestimated compared to the experiments. This discrepancy could be attributed to i). ignoring the contributions of a large number of non-local phonon modes, and ii). approximating the supercell using the cluster model in the calculation of the ZFS. Despite these deficiencies, the decreasing trend in D with increasing temperature is correctly captured by our present calculations, and the difference between the two isotopes is also well reproduced, which again solidifies the phenomenological model that we've been fitting throughout this work.

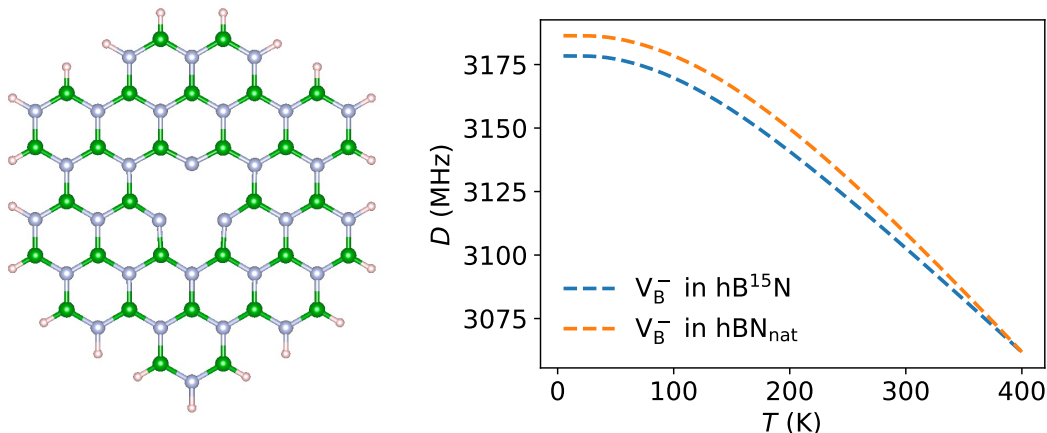


FIG. S4. Temperature dependence of the zero field splitting of both hB¹⁵N and hBN_{nat} (right), computed from the cluster model (left) by only considering the second-order coupling between spin and local phonon modes near the defect. Here, we aligned the two curves at around 400 K for a better comparison with experiments.

We also note that Péter et al. [15] have studied the effects of lattice strain on the ZFS. From Supplementary Fig. 2 of Ref. [15], we can extract that the first-order contribution to the ZFS's temperature dependence is also negligible, which aligns with our expectations. Their supplementary Fig. 4b also corroborates our conclusion that the first-order contribution to the hyperfine tensor is negligible.

IV.4. Spin Relaxation Time

The spin relaxation of a defect could be credited to multiple possible mechanisms. Different mechanisms could play important roles in different temperature ranges. Since the ZFS of V_B^- in hBN is ~ 3.5 GHz, it's well below the typical phonon energies of hBN [12]. For temperatures well above 0 K, the one-phonon (direct) process can be safely ignored. Therefore, we mainly focus on the two-phonon processes. For the standard Orbach process [16], it's also unlikely to

happen for V_B^- , because the lowest-lying excited state is ~ 800 meV higher than the triplet ground state [17], well beyond the phonon cutoff frequency which is ~ 200 meV in hBN [18].

One other possible two-phonon process is the Raman scattering process and it could be driven by either first-order or second-order spin-phonon interactions. Ref. [19] proposed a criterion to distinguish which of the two is dominant, namely the ratio between these two contributions, i.e., $(2\pi D/\omega)^2$, where D is the ZFS and ω is the acoustic phonon energy. Ref. [19] also showed that for NV^- center in diamond, $(2\pi D/\omega)^2 \sim 10^{-7}$ and therefore the dominant driving force is second-order spin-phonon interactions. For V_B^- in hBN, we can also estimate its value as 10^{-5} , where we've taken the acoustic phonon energy as ~ 26 meV [20]. We can, therefore, conclude safely that the major mechanism responsible for the spin relaxation in V_B^- is the Raman scattering driven by second-order spin-phonon interactions, and our analysis is corroborated by Ref. [12].

In this scenario, the spin relaxation rate can be modeled as

$$\Gamma(T) = 1/T_1 = \sum_i A_i n_i (n_i + 1) + A_S, \quad (\text{S4})$$

which is a more general form than Eq. 4 in the main text. Since we only identified a single representative phonon mode for the temperature dependence of ZFS, we only fit a single set of A, n .

V. ODMR CONTRAST AND MICROWAVE LOSS

In main text we mention the ODMR contrast exhibits a maximum around 210 K for V_B^- in both hBN samples, and here we will demonstrate that this contrast feature is not correlated with the microwave loss during transmission. We perform an S-parameter transmission efficiency test (S12) on our coplanar waveguide in the cryostat using a vector network analyzer (Agilent Technologies N5239A) within temperature range from 10 K to 350 K. The transmitted power is reduced by 4-6.5 dB in the frequency range from 3100 MHz to 3500 MHz which covers the resonant frequency of the $|m_s = 0\rangle \leftrightarrow |m_s = -1\rangle$ transition in our experiment (Fig. 1c,d in main text). We take the average value in the frequency range and plot it as a gray line in Fig. S5. The transmission efficiency result exhibits a monotonic decrease with increasing temperature. In comparison, the ODMR contrasts of the $|m_s = 0\rangle \leftrightarrow |m_s = -1\rangle$ transition of V_B^- in $h^{10}B^{15}N$ and hBN_{nat} flakes firstly increases, peaks around 210 K and then decreases as temperature going up. As a result, the ODMR contrast behavior of V_B^- can not be explained by the transmission loss in this case. We note that further investigation is required to understand the mechanism of the V_B^- ODMR contrast temperature dependence.

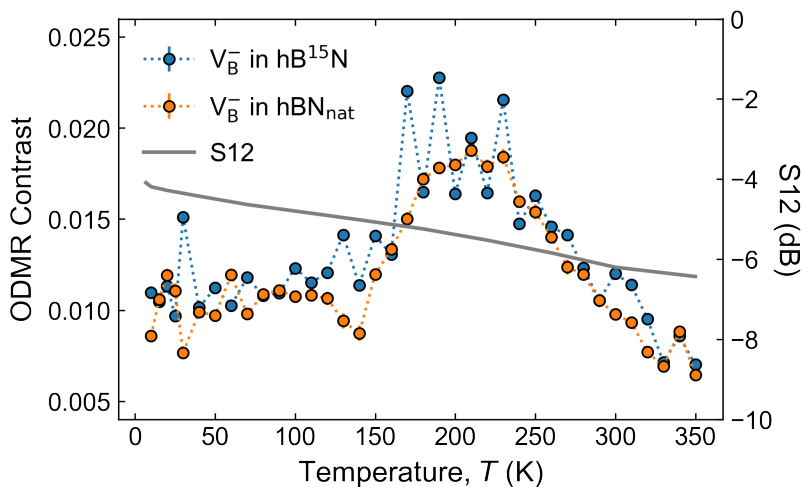


FIG. S5. **ODMR contrast and S12 test with temperature dependence.** The ODMR contrasts of the $|m_s = 0\rangle \leftrightarrow |m_s = -1\rangle$ transition of V_B^- in $h^{10}B^{15}N$ and hBN_{nat} flakes are labeled with blue and orange respectively. The contrast reaches its maximum around 210 K for both isotopes. The S12 value is taken by the average result in 3100-3500 MHz frequency range which covers the resonant frequency of the $|m_s = 0\rangle \leftrightarrow |m_s = -1\rangle$ transition from 10 K to 350 K (Fig. 1c,d in main text).

VI. NUCLEAR SPIN POLARIZATION

VI.1. Interaction Hamiltonian for $V_{\bar{B}}$ and nuclear spins

To understand the nuclear spin polarization process, we must first derive the Hamiltonian that governs the $V_{\bar{B}}$ and nuclear spins interaction. The $V_{\bar{B}}$ electronic spin-1 operators can be written as

$$S_z = \begin{bmatrix} 1 & 0 & 0 \\ 0 & 0 & 0 \\ 0 & 0 & -1 \end{bmatrix}, S_x = \frac{1}{\sqrt{2}} \begin{bmatrix} 0 & 1 & 0 \\ 1 & 0 & 1 \\ 0 & 1 & 0 \end{bmatrix}, S_y = \frac{1}{\sqrt{2}i} \begin{bmatrix} 0 & 1 & 0 \\ -1 & 0 & 1 \\ 0 & -1 & 0 \end{bmatrix}. \quad (S5)$$

Here we define the spin raising and lowering operators for the $V_{\bar{B}}$ electron spin as

$$S_+ = \sqrt{2} \begin{bmatrix} 0 & 1 & 0 \\ 0 & 0 & 1 \\ 0 & 0 & 0 \end{bmatrix} = S_x + iS_y, S_- = \sqrt{2} \begin{bmatrix} 0 & 0 & 0 \\ 1 & 0 & 0 \\ 0 & 1 & 0 \end{bmatrix} = S_x - iS_y, \quad (S6)$$

and consequently the $V_{\bar{B}}$ spin operators can be expressed as

$$S_x = \frac{S_+ + S_-}{2}, S_y = \frac{S_+ - S_-}{2i}. \quad (S7)$$

Similarly, for ^{15}N nuclear spins, we have operators

$$I_z = \frac{1}{2} \begin{bmatrix} 1 & 0 \\ 0 & -1 \end{bmatrix}, I_x = \frac{1}{2} \begin{bmatrix} 0 & 1 \\ 1 & 0 \end{bmatrix}, I_y = \frac{1}{2i} \begin{bmatrix} 0 & 1 \\ -1 & 0 \end{bmatrix}. \quad (S8)$$

$$I_+ = \begin{bmatrix} 0 & 1 \\ 0 & 0 \end{bmatrix} = I_x + iI_y, I_- = \begin{bmatrix} 0 & 0 \\ 1 & 0 \end{bmatrix} = I_x - iI_y, \quad (S9)$$

$$I_x = \frac{I_+ + I_-}{2}, I_y = \frac{I_+ - I_-}{2i}. \quad (S10)$$

The hyperfine interaction term between $V_{\bar{B}}$ and three ^{15}N nuclear spins takes the form $\sum_{j=1}^3 \mathbf{SA}^j \mathbf{I}^j$ where the hyperfine parameters tensor \mathbf{A} for a single nuclear spin can be expressed as

$$\mathbf{A} = \begin{bmatrix} A_{xx} & A_{xy} & A_{xz} \\ A_{yx} & A_{yy} & A_{yz} \\ A_{zx} & A_{zy} & A_{zz} \end{bmatrix} = \begin{bmatrix} A_{xx} & A_{xy} & 0 \\ A_{yx} & A_{yy} & 0 \\ 0 & 0 & A_{zz} \end{bmatrix}. \quad (S11)$$

Here the \hat{z} -axis is defined along the c -axis of hBN (perpendicular to the lattice plane, see main text Figure. 1), \hat{x} and \hat{y} lie in the lattice plane, with \hat{x} oriented along one of the three in-plane nitrogen bonds. Due to the mirror symmetry of $V_{\bar{B}}$ with respect to the $\hat{x} - \hat{y}$ plane, the four terms $A_{xz} A_{yz} A_{zx} A_{zy}$ vanish [9, 21]. We can then expand the

hyperfine interacting Hamiltonian to its full form

$$\begin{aligned}
\sum_{j=1}^3 \mathbf{SA}^j \mathbf{I}^j &= \sum_{j=1}^3 (A_{zz}^j S_z I_z^j + A_{xx}^j S_x I_x^j + A_{yy}^j S_y I_y^j + A_{xy}^j S_x I_y^j + A_{yx}^j S_y I_x^j) \\
&= \sum_{j=1}^3 [A_{zz}^j S_z I_z^j + \frac{1}{4} A_{xx}^j (S_+ + S_-)(I_+^j + I_-^j) - \frac{1}{4i} A_{yy}^j (S_+ - S_-)(I_+^j - I_-^j) \\
&\quad + \frac{1}{4i} A_{xy}^j (S_+ + S_-)(I_+^j - I_-^j) + \frac{1}{4i} A_{yx}^j (S_+ - S_-)(I_+^j + I_-^j)] \\
&= \sum_{j=1}^3 [A_{zz}^j S_z I_z^j + \frac{A_{xx} + A_{yy}}{4} (S_+ I_-^j + S_- I_+^j) \\
&\quad + (\frac{A_{xx} - A_{yy}}{4} + \frac{A_{xy}}{2i}) S_+ I_+^j + (\frac{A_{xx} - A_{yy}}{4} - \frac{A_{xy}}{2i}) S_- I_-^j].
\end{aligned} \tag{S12}$$

Note that $A_{xy} = A_{yx}$ from the symmetry in the last step[9]. Finally, since $(S_+ I_-^j)^\dagger = (S_- I_+^j)$ and $(S_- I_-^j)^\dagger = (S_- I_-^j)$, we can further simplify the expression to the form

$$\sum_{j=1}^3 \mathbf{SA}^j \mathbf{I}^j = \sum_{j=1}^3 [A_{zz}^j S_z I_z^j + (A_1^j S_+ I_-^j + h.c.) + (A_2^j S_+ I_+^j + h.c.)], \tag{S13}$$

where we define $A_1^j = \frac{1}{4}(A_{xx}^j + A_{yy}^j)$ and $A_2^j = \frac{1}{4}(A_{xx}^j - A_{yy}^j) + \frac{1}{2i} A_{xy}^j$.

VI.2. Spin population transfer near esLAC

To enable resonant spin exchange between electronic and nuclear spins, we apply an external magnetic field $B_z \approx 760$ under which the energy levels corresponding to V_B^- excited state $|m_s = 0\rangle$ and $|m_s = -1\rangle$ are nearly degenerate (known as electronic spin level anti-crossing, esLAC) [21–23]. The hyperfine interaction Hamiltonian is in full display as written in the previous section since the secular approximation is no longer valid. In the equation S13, the more dominant term $(A_1^j S_+ I_-^j + h.c.)$ leads to electron-nuclear spin flip-flop, $|m_s = 0, m_I = \downarrow\rangle \leftrightarrow |m_s = -1, m_I = \uparrow\rangle$, while the secondary term $(A_2^j S_+ I_+^j + h.c.)$ connects the other two states, $|m_s = 0, m_I = \uparrow\rangle \leftrightarrow |m_s = -1, m_I = \downarrow\rangle$ (main text Fig. 4b inset).

As a result, the ^{15}N nuclear spin population will preferentially transfer to $|m_I = \uparrow\rangle$ state when a strong optical polarization continuously pumps the electronic spin from $|m_s = \pm 1\rangle$ to $|m_s = 0\rangle$.

VI.3. Quantifying polarization

To quantitatively describe the nuclear spin polarization as a function of temperature, we record the ESR spectra while sweeping the laser power, i.e., the optical pumping rate. We extract the nuclear spin polarization of the nearest three ^{15}N by first assuming each nuclear spin is individually prepared to $|m_I = \uparrow\rangle$ with probability $P(|\uparrow\rangle)$ and $|m_I = \downarrow\rangle$ with probability $1 - P(|\uparrow\rangle)$. The energy sublevels accounting for the three ^{15}N spins should effectively follow a binomial distribution with $n = 3$, the total number of a sequence of independent events. For a random variable X defined as the number of ^{15}N nuclear spins being measured to be $|m_I = \uparrow\rangle$ in a single observation, the probability mass function is

$$\Pr(X = k) = \binom{n}{k} P^k (1 - P)^{3-k}. \tag{S14}$$

For example, the four possible nuclear spin configurations correspond to $\sum m_I = -\frac{3}{2}, -\frac{1}{2}, \frac{1}{2}, \frac{3}{2}$ and $X = 0, 1, 2, 3$. Therefore, the theoretical probability distribution follows $\{\binom{3}{3}(1 - P)^3 : \binom{3}{2}P(1 - P)^2 : \binom{3}{1}P^2(1 - P) : \binom{3}{0}P^3\} = \{(1 - P)^3 : 3P(1 - P)^2 : 3P^2(1 - P) : P^3\}$. When there is no nuclear spin polarization ($P = 0.5$), we obtain amplitudes $\{1 : 3 : 3 : 1\}$ for the ESR spectra.

To quantitatively extract the nuclear polarization, we first fit the ESR spectrum using the sum of four equally spaced Lorentzian distribution whose amplitude follows the aforementioned ratio. However, we note that the gyromagnetic

ratio for ^{15}N is negative, which reverses the order of the sublevels in the ESR spectrum. In this case, for the V_{B}^- transition between electronic $|m_s = 0\rangle$ and $|m_s = +1\rangle$ states, the lowest-frequency resonance corresponds to $\sum m_I = \frac{3}{2}$ or $X = 3$.

-
- [1] E. Janzen, H. Schutte, J. Plo, A. Rousseau, T. Michel, W. Desrat, P. Valvin, V. Jacques, G. Cassabois, B. Gil, and J. H. Edgar, *Advanced Materials*, 2306033 (2023).
- [2] Y. Huang, E. Sutter, N. N. Shi, J. Zheng, T. Yang, D. Englund, H.-J. Gao, and P. Sutter, *ACS Nano* **9**, 10612 (2015).
- [3] P. Giannozzi, S. Baroni, N. Bonini, M. Calandra, R. Car, C. Cavazzoni, D. Ceresoli, G. L. Chiarotti, M. Cococcioni, I. Dabo, *et al.*, *Journal of Physics: Condensed Matter* **21**, 395502 (2009).
- [4] P. Giannozzi, O. Andreussi, T. Brumme, O. Bunau, M. B. Nardelli, M. Calandra, R. Car, C. Cavazzoni, D. Ceresoli, M. Cococcioni, *et al.*, *Journal of Physics: Condensed Matter* **29**, 465901 (2017).
- [5] J. P. Perdew, K. Burke, and M. Ernzerhof, *Physical Review Letters* **77**, 3865 (1996).
- [6] L. Chaput, A. Togo, I. Tanaka, and G. Hug, *Phys. Rev. B* **84**, 094302 (2011).
- [7] H. Tang, A. R. Barr, G. Wang, P. Cappellaro, and J. Li, *The Journal of Physical Chemistry Letters* **14**, 3266 (2023).
- [8] W. Paszkowicz, J. Pelka, M. Knapp, T. Szyszko, and S. Podsiadlo, *Applied Physics A* **75**, 431 (2002).
- [9] V. Ivády, G. Barcza, G. Thiering, S. Li, H. Hamdi, J.-P. Chou, Ö. Legeza, and A. Gali, *npj Computational Materials* **6**, 41 (2020).
- [10] J. Heyd, G. E. Scuseria, and M. Ernzerhof, *The Journal of Chemical Physics* **118**, 8207 (2003).
- [11] T. Biktagirov, W. G. Schmidt, and U. Gerstmann, *Physical Review Research* **2**, 022024 (2020).
- [12] S. Mondal and A. Lunghi, *npj Computational Materials* **9**, 120 (2023).
- [13] C. Adamo and V. Barone, *The Journal of Chemical Physics* **110**, 6158 (1999).
- [14] F. Neese, F. Wennmohs, U. Becker, and C. Riplinger, *The Journal of Chemical Physics* **152** (2020).
- [15] P. Udvarhelyi, T. Clua-Provost, A. Durand, J. Li, J. H. Edgar, B. Gil, G. Cassabois, V. Jacques, and A. Gali, *npj Computational Materials* **9**, 150 (2023).
- [16] R. Orbach, *Proceedings of the Royal Society of London. Series A. Mathematical and Physical Sciences* **264**, 458 (1961).
- [17] J. R. Reimers, J. Shen, M. Kianinia, C. Bradac, I. Aharonovich, M. J. Ford, and P. Piecuch, *Physical Review B* **102**, 144105 (2020).
- [18] S. Reich, A. Ferrari, R. Arenal, A. Loiseau, I. Bello, and J. Robertson, *Physical Review B* **71**, 205201 (2005).
- [19] M. C. Cambria, A. Norambuena, H. T. Dinani, G. Thiering, A. Gardill, I. Kemeny, Y. Li, V. Lordi, A. Gali, J. R. Maze, and S. Kolkowitz, *Phys. Rev. Lett.* **130**, 256903 (2023).
- [20] B. Krummheuer, V. M. Axt, and T. Kuhn, *Physical Review B* **65**, 195313 (2002).
- [21] X. Gao, S. Vaidya, K. Li, P. Ju, B. Jiang, Z. Xu, A. E. L. Allcca, K. Shen, T. Taniguchi, K. Watanabe, *et al.*, *Nature Materials* **21**, 1024 (2022).
- [22] R. Gong, X. Du, E. Janzen, V. Liu, Z. Liu, G. He, B. Ye, T. Li, N. Y. Yao, J. H. Edgar, *et al.*, *Nature Communications* **15**, 104 (2024).
- [23] N. Mathur, A. Mukherjee, X. Gao, J. Luo, B. A. McCullian, T. Li, A. N. Vamivakas, and G. D. Fuchs, *Nature Communications* **13**, 3233 (2022).